



TITLE:

Periodic solar wind forcing due to recurrent coronal holes during 1996–2009 and its impact on Earth's geomagnetic and ionospheric properties during the extreme solar minimum

AUTHOR(S):

Tulasi Ram, S.; Liu, C. H.; Su, S.-Y.

---

CITATION:

Tulasi Ram, S. ...[et al]. Periodic solar wind forcing due to recurrent coronal holes during 1996–2009 and its impact on Earth's geomagnetic and ionospheric properties during the extreme solar minimum. *Journal of Geophysical Research* 2010, 115: ...

ISSUE DATE:

2010-12

URL:

<http://hdl.handle.net/2433/137410>

RIGHT:

©2010. American Geophysical Union.; この論文は出版社版ではありません。引用の際には出版社版をご確認ご利用ください。; This is not the published version. Please cite only the published version.

1    **Periodic solar wind forcing due to recurrent Coronal Holes during 1996-2009 and**  
2    **its impact on Earth's geomagnetic and ionospheric properties during extreme solar**  
3    **minimum**

4    S. Tulasi Ram<sup>1</sup>, C. H. Liu<sup>2</sup>, and S.-Y. Su<sup>3</sup>

5    <sup>1</sup> Institute of Astronomy and Astrophysics, Academia Sinica, Taipei, Taiwan (R.O.C).

6    <sup>2</sup> Academia Sinica, Taipei, Taiwan (R.O.C).

7    <sup>3</sup> Institute of Space Science, National Central University, Chung-li, Taiwan (R.O.C).

8

9    **Abstract**

10    The periodicities in the area of Coronal Hole (CH) regions on the solar disk and the solar  
11    wind (SW) high speed streams (HSS) have been studied, for the first time, during the  
12    complete solar cycle 23 (SC 23) from 1996 to 2009 using the solar EUV image data from  
13    SOHO, STEREO satellites and ACE solar wind-magnetic data. Both the solar wind  
14    velocity and the area of CH regions consistently exhibit large values during the declining  
15    phase and the minimum of SC 23 (2003 to 2009) due to equatorward extended holes  
16    and/or low-latitude isolated holes. Further, the SW velocity and CH area exhibit greater  
17    tendency for sub-harmonic (13.5-day and 9-day) periodicities during the declining phase  
18    and solar minimum. The response of Earths' geomagnetic and ionospheric properties to  
19    these periodicities associated with Co-rotating Interaction Regions (CIRs) in high speed  
20    solar wind streams is studied with focus during the extremely low solar activity period of  
21    2008. The sub-harmonic oscillations in both day and night side ionospheric electron  
22    density are found to correlate well with the oscillations in SW and Kp during 2008. The  
23    topside ionospheric response (above 350 km) appears to be dominated by the changes in  
24    the plasma temperature and/or scale height and exhibits coherent enhancements with the

oscillations in geomagnetic activity during both the day and night times. However, the electron density response between 200 and 350 km altitudes is dominated by the changes in the neutral composition and exhibits significant latitudinal, local time and seasonal variations. The results are discussed in light of equatorward wind perturbations during enhanced geomagnetic activity and summer-to-winter transequatorial neutral wind patterns.

## 1. Introduction

Understanding the complex interplay between the solar variability and space weather is very important for forecasting the disturbances in the Geospace environment that can affect the astronauts in space, payloads on board the satellites, space based communication and navigational systems as well as ground based power grid systems. The Coronal Mass Ejections (CMEs) and solar flares are the sources of high energy particles and are of primary importance because of their huge and immediate impact on the Earth. Further, the Coronal Holes (CHs) on the Sun, the principal sources of high speed solar wind particles, are another important source of geomagnetic disturbances on the Earth. The Coronal Holes are mainly unipolar magnetic field regions on the Sun with one foot print of field lines are attached to Sun and other are extending in to the interplanetary space giving rise to emission of high-speed solar wind streams [Krieger et al., 1973]. The proton density in CHs is typically 2 – 3 times lower than that of the quiet Sun and the temperature is around  $10^5 - 10^6$  K [Munro and Withbroe, 1972]. Due to their low density and emission measure, CHs can be identified as dark areas on X-ray and EUV images of the Sun and dominant unipolar regions on magnetograms [Reeves and Parkinson, 1970; Wiegmann and Solanki, 2004]. When the interplanetary magnetic

field is oriented southward, strong coupling between the magnetized plasma within the high speed streams and Earth's magnetosphere results in transfer of mass, momentum and energy producing geomagnetic disturbances. Since the CHs rotate almost rigidly with the Sun, they produce recurrent high speed streams and geomagnetic disturbances in the Geospace environment [Timothy et al. 1975 and Tsurutani et al. 1995].

The coronal holes and solar wind streams undergo systematic variations over the 11-year solar cycle. Through much of the cycle, the Sun's polar region is dominated by coronal holes, the sources of large, persistent and fast solar wind streams with an average bulk speed of 500 – 800 km/s [Philips et al., 1995]. During the solar minimum, the polar holes became large and extend into equatorial and low latitude regions with some tongue-like extensions [Krieger et al., 1973; Sheeley and Harvey, 1981]. In addition to fast streams from polar holes, the solar wind has also dense low-speed streams (300 – 400 km/s) from the closed field regions near the equator, known as equatorial coronal streamer belt. As the streams travel in the interplanetary space, the high-speed streams catch the slow-speed streams and create regions of enhanced density and magnetic field, called co-rotating interaction regions (CIRs) [Tsurutani et al. 1995]. When the coronal high speed wind interacts with the preceding slow solar wind, forward and reverse shocks often form at the CIR boundaries. The CIR interfaces can be characterized by a relatively sharp density drop, temperature rise and a sharp increase in the solar wind bulk velocity. CIRs are especially prominent during the declining phase of the solar cycle, when the heliospheric magnetic field has a well-developed sector structure and coronal holes may extend to low latitudes [Richardson 2004].



70           The fast streams from the CHs and CIR interfaces have a tendency to repeat for  
71 several solar rotations producing recurrent geomagnetic activity at 27-day periodicity.  
72 However, recent investigations by Temmer et al. 2007 and Gibson et al. 2009 have  
73 elucidated that the solar wind velocity and geomagnetic properties also exhibit sub-  
74 harmonic solar rotational periodicities at 13.5-day, 9-day and even shorter periods during  
75 the descending and minimum phase of solar cycle 23. In response, the Earth's upper  
76 atmospheric properties such as thermospheric density and composition, plasma  
77 temperature, and electron density are also found to oscillate with the same periodicities  
78 [Lei et al., 2008a; Crowley et al., 2008; Sojka et al., 2009; Tulasi Ram et al., 2010].

79           The electron density in the ionosphere responds significantly to the changes in the  
80 thermosphere composition, neutral density, temperature, neutral winds as well as the  
81 electric fields, which in turn greatly varies with latitude, altitude, local time, season and  
82 the phase of the geomagnetic activity. Because of various neutral and electro-dynamic  
83 coupling processes are involved, the global ionospheric response to geomagnetic storms  
84 is much complex and been the subject of extensive investigations by both case studies as  
85 well as model simulations during the past 3-4 decades [Prolss, 1980; Fuller-Rowell et al.,  
86 1994, 1996; Buansanto 1999; Mendillo 2006 and the references therein]. However, the  
87 earlier studies on the altitudinal response of global ionosphere to geomagnetic storms  
88 were mostly based on the model simulations due to lack of global observations of vertical  
89 electron density profiles. Although the amplitude is smaller, the solar wind interfaces  
90 produce ionospheric changes similar to those associated with isolated geomagnetic  
91 storms [Mendillo and Schatter, 1983]. Hence, the short-period recurrent geomagnetic  
92 disturbances associated with periodic solar wind forcing during the low solar activity

periods provide an opportunity for a comprehensive investigation on the global scale ionospheric response to minor geomagnetic storms.

Therefore, the objective of the present investigation is for further understanding of periodic solar wind streams from recurrent coronal holes and its impact on Earth's geomagnetic and ionospheric properties. In this context, we first present the results of a systematic study of periodicities in the solar wind velocity and the area of coronal hole regions during the complete period of solar cycle 23. Secondly, we focus our investigation on extremely low solar activity period of 2008 to study the modulation of interplanetary solar wind parameters due to recurrent coronal holes and its imprints on the Earth's geomagnetic and ionospheric properties. Further, we present the seasonal dependence on the ionospheric response to recurrent geomagnetic activity associated with periodic solar wind forcing at different latitudinal-altitudinal regions.

## 2. Results and Discussion

### 2.1 Periodicities in the Solar wind velocity and the area of Coronal hole regions during the solar cycle 23

The solar wind (SW) velocity data from WIND and Atmospheric Composition Explorer (ACE) satellites during the period from the previous solar minimum to the minimum of SC23 (1996 to 2009), available through National Space Science Data Center's OMNIWeb interface (<http://nssdc.gsfc.nasa.gov/omniweb/>) has been considered in this study. The daily mean solar wind velocity data of 5114 consecutive days (14 – years) has been subjected to Morlet wavelet analysis to identify the various periodicities during different phases of the SC23. Figure 1(a) shows the daily variation of SW velocity (light blue line) and its 27-day running mean variation (thick blue line) from the

years 1996 to 2010. The daily variation of F10.7 solar flux (pink line) and its 27-day running mean variation are also shown in the same panel with right hand side scale to represent as a proxy to the solar activity variation during the SC23. It can be observed from this figure that the mean SW velocity during the previous solar minimum and the ascending phase of SC23 (1996 to late 2002) generally varies around 400 km/s (indicated by black dashed line). However, the mean SW velocity exhibits significantly larger values (420 to 600 km/s) during the descending phase of the SC23 (2003 to 2009) than ascending phase of SC23. This indicates that the source regions of high speed streams on the Sun are more populated and geo-effective during the descending phase of solar cycle than the ascending phase.

The Morlet wavelet power spectrum of daily mean SW velocity during the complete solar cycle (SC 23) is presented in the bottom panel [Fig. 1(b)]. It can be observed from this figure that the SW velocity exhibits periodicities at solar rotational (27-day) and its sub-harmonic periods (13.5-, 9- and 6.8-days) as indicated by horizontal pink dashed lines. The most interesting observation from the wavelet analysis is that the SW velocity has greater tendency to exhibit sub-harmonic solar rotational periodicities (13.5-, 9- and 6.8-days) during the same period where the SW velocity in general exhibits large values in Fig. 1(a), i.e., during the descending phase of SC23 (2003 to 2009). While these periodicities may also be observed during previous solar minimum and ascending phase of SC23, they occur occasionally and only for short periods. However during the descending phase, these sub-harmonic periodicities are observed for long and continuous patches with large spectral intensities.

138           The periodicities in the SW velocity can be explained by the longitudinal  
139 distribution of CHs on the Sun in a straight forward manner. For example, Temmer et al.  
140 [2007] and Lei et al. [2008b] have shown that the 9-day periodicity in the SW velocity in  
141 2005 is mainly due to a triad of coronal holes at approximately  $120^\circ$  apart in heliographic  
142 longitude that persist for several rotations. Thus, with a view to further investigate the  
143 spatial distribution of CHs on the Sun and the resultant periodicities in the SW properties  
144 during different phase of SC23, the extreme ultraviolet images of the Sun have been  
145 analyzed to compute the daily fractional CH area as described in Vrsnak et al. [2007] and  
146 Temmer et al. [2007]. The daily images of the Sun at  $195 \text{ \AA}$  from Extreme Ultraviolet  
147 Imaging Telescope (EIT) on board the Solar and Heliospheric Observatory (SOHO)  
148 during the period from June 1996 to 2006 and from Extreme Ultraviolet Imager (EUVI)  
149 on board the Solar Terrestrial Relations Observatory (STEREO) during the period from  
150 2007 to 2009 were considered in this study.

151           The coronal holes on the Sun are identified by threshold intensity detection  
152 method described in Krista and Gallagher [2009]. In this method, the intensity  
153 distribution (histogram) of the  $195 \text{ \AA}$  image is constructed and the intensity  
154 corresponding to the maximum in the histogram is considered as the quiet Sun intensity.  
155 The threshold value for the detection of CHs is defined as the local minima in the  
156 intensity histogram that are located within 30-70 % of the quiet Sun intensity and are  
157 wider than 6 digital numbers (DNS). For those cases when the well defined minima  
158 cannot be noticed, 40 % of the quiet Sun intensity is considered as the threshold to  
159 identify the CHs. Since the thresholds are determined depending on the quiet Sun  
160 intensity, this method is suitable during different phases of the solar cycle regardless of

the change in the overall intensity of Sun as well as independent of instrumental intensity settings [Krista and Gallagher, 2009].

Figure 2 shows the typical examples of SOHO-EIT images at 195 Å during ascending and descending phases of the SC 23 to illustrate the method of identification of CHs on solar images for the computation of fractional CH area. The area covered by the CHs in the central meridian slice between -10° and 10° heliographic longitudinal range and between -60° and 60° heliographic latitudes (the area covered by pink contour line) is computed for each day using the equation. (1).

$$\text{Fractional CH area} = \frac{\text{No. of pixels covered by CH in } [\pm 10^\circ \text{ h.long}, \pm 60^\circ \text{ h.lat}]}{\text{Total No. of pixels in } [\pm 10^\circ \text{ h.long}, \pm 60^\circ \text{ h.lat}]} \text{ ---- (1)}$$

Here, the CH area between  $\pm 60^\circ$  heliographic latitudes is only considered in order to emphasize the effect of CHs which are extended equatorward as well as low-mid latitude isolated CHs. In this analysis, one solar disk image at 195 Å for each day around 13 UT is considered because of the satellite sampling time of SOHO and maximum availability of data at 13 UT. For the days on which the image data was missing, we used an adjacent longitudinal stripe from the previous/next day image whichever is available. Further missing/bad data for less than 5 consecutive days are linearly interpolated to compute the wavelet power spectrum (WPS). However, there are still some data gaps in the SOHO-EIT data, hence, the WPS is computed only on continuous data segments of length more than 50 days.

Figure 3(a) shows the daily variation of fractional CH area (light blue line) from 1996 to 2010 and its 27-day running mean variation (dark blue line). The corresponding wavelet spectrum of CH area is presented in Fig. 3(b). The significant observation from Fig. 3(a) is that the CH area computed between  $\pm 60$  heliographic latitudes also exhibits

large values from 2003 to 2009. The large values of SW velocity [Fig. 1(a)] and CH area [Fig. 3(a)] observed during the same period clearly indicates that the equatorward extension of polar holes and low latitude (probably isolated) coronal holes are more prominent during the descending phase of SC23 from 2003 to 2009. The fast solar wind streams from these coronal holes engulfed the Earth's environment resulting in large values of SW velocity as measured by ACE at L1 point. Further, the wavelet spectrum of CH area [Fig. 3(b)] also exhibits greater tendency to sub-harmonic periodicities at 13.5 and 9-days similar to that of SW velocity during the descending phase of SC23. These results indicate that a two to three large CH regions (either equatorward extended holes or isolated holes) that are longitudinally separated and persistent for several solar rotations have produced 13.5-day or 9-day periodicities in the CH area. The fast SW stream trajectories from these CHs engulf the geo-space environment and produce similar periodicities in SW velocity. Further, this feature is more prominent during the descending phase of the SC23. However, the exact one-to-one correlation of spectral intensities between CH area and SW may not be expected because the solar wind trajectories may some times perturbed by energetic events such as CMEs, solar flares and solar energetic particle events from the Sun. Even though the previous solar minimum (1996-1998) period has nearly the same solar activity (F10.7 solar flux) levels as the minimum of SC 23 (2005-2009), the values of both CH area and SW velocity are smaller during the previous solar minimum and the sub-harmonic periodicities are only occasionally observed for short periods.

## 2.2 Periodic modulation of interplanetary SW parameters and their imprints on Earth's geomagnetic activity during extreme solar minimum period, 2008.

We now focus our attention on the sub-harmonic periodicity of 9-day period as a diagnostic tool to study the periodic modulation in the interplanetary solar wind properties and their imprints on Earth's geomagnetic properties. The reasons for choosing the 9-day periodicity are explained in the next section. With a view to investigate the 9-day periodicity in the fractional CH area and its modulation on the interplanetary solar wind properties, the ACE's high resolution (64-second) Level-2 data during the solar minimum period in 2008 are carefully examined. This period was selected because the wavelet of both CH area and SW velocity exhibits strong 9-day periodicity during most of the year 2008 and also because of the availability of Formosat-3/COSMIC vertical electron density profile data to further study the seasonal dependence on latitudinal and altitudinal response of ionospheric electron density to this 9-day periodicity.

Figures 4(a) to (h) shows the fractional CH area derived from STEREO-EUVI images along with SW bulk velocity, SW magnetic field magnitude,  $|B|$ , SW proton temperature, SW proton density, vertical component, IMF  $B_z$ , symmetrical ring current index, SymH and geomagnetic activity index, Kp, respectively, during 2008. Although the 9-day periodicity in SW velocity can be seen almost throughout the year 2008, the data pertaining to the day numbers 1 to 120 are only shown in figure 4 for better visibility. It can be seen from this figure that the variation of SW velocity corresponds well with the variation of CH area with a phase delay of 2-3 days. This phase delay generally agrees with the travelling time of SW particles from the source to orbit of ACE

230 at L1-point. A careful examination of figures 4(b) to 4(e) reveals that the interplanetary  
231 SW properties exhibit the signatures of a series of co-rotating interaction regions (CIRs)  
232 during this period. It can be observed from these figures that, every sharp increase in SW  
233 velocity corresponds with a sharp increase in magnetic field magnitude, sharp increase in  
234 SW proton temperature and a sharp decrease in SW proton density, which are the  
235 signatures of CIR stream interface [Richardson et al. 1996, 1998, Tsurutani et al. 2006,  
236 2008, Choi et al. 2009]. Further, the impulse type increase-and-decrease of magnetic  
237 field magnitude, proton density preceding-and-after the increase of SW velocity indicates  
238 the signatures of forward and reverse shocks associated with CIRs [Kennel et al. 1985,  
239 Tsurutani et al. 2006, 2008 and Choi et al. 2009]. Lei et al. [2010] have made a detailed  
240 investigation on the interplanetary solar wind parameters during 2008 and identified the  
241 presence of 38 CIRs in the entire year 2008 using the method described in McPherron et  
242 al. [2009]. Thus, the results from the figures 4(a)-(e) and the results from Lei et al.  
243 [2010] indicate that a series of CIRs are formed at quasi 9-day periodicity because of the  
244 interaction of fast solar wind stream trajectories from the equatorward extended or low-  
245 latitude (probably isolated) coronal holes with the preceding ambient slow solar wind  
246 streams. The resultant CIR structures of enhanced density and magnetic field regions  
247 impinge upon the Earth's magnetosphere and can trigger recurrent geomagnetic activity  
248 at quasi 9-day periodicity. For instance, from Figs. 4(g), it can be observed that a series  
249 of recurrent geomagnetic storms of weak to moderate intensities ( $SymH \leq -30$  to  $-50$  nT)  
250 occurred throughout this period. A good correlation between the large positive and  
251 negative excursions of IMF Bz and the corresponding decrease in SymH index as well as  
252 simultaneous increase in Kp-index can be observed from figures 4(f), 4(g) and 4(h).



Because of highly oscillatory nature of  $B_z$  component with in CIRs [Fig. 4(f)], the resultant geomagnetic storms are typically only weak to moderate intensity. However, the recovery phases of these storms are elongated for several days or more as can be seen from Fig. 4(g).

The Lomb-Scargle (LS) amplitude spectra [Lomb, 1976; Scargle, 1982] of various parameters that described previously such as CH area, SW velocity, SW magnetic field magnitude ( $|B|$ ), IMF  $B_z$ , SymH index, Kp-Index during the entire year of 2008 are presented in Figs. 5(a) to (f) respectively. Further, the LS spectra of Total Solar Irradiance (TSI) and EUV irradiance at 5-105 nm wavelengths are also shown for comparison in Figs. 5(g) and 5(h), respectively. Here, the TSI data is obtained from the measurements of TIM instrument on board the SORCE satellite and EUV irradiance data is obtained from the level-3 data products of Solar EUV Experiment (SEE) on board the TIMED satellite. It can be clearly observed from this figure that the CH area, solar wind parameters (SW velocity and SW magnetic field) as well as the geomagnetic activity indices (SymH and Kp indices) exhibit pronounced spectral peaks at 13.5 and 9-day periods. Further, the 9-day periodicity is strongly present in SW total magnetic field  $|B|$  due to compression effects at the beginning of the CIRs. However, the 9-day periodicity is absent in the vertical component  $B_z$ . This could be due to the large positive and negative fluctuations in IMF  $B_z$  [Fig. 4(f)] at stream-stream compression regions, which are the typical signatures of CIRs as described by Tsurutani 2005, 2006 and references therein. On the other hand, the Total Solar Irradiance (TSI) and EUV irradiance do not exhibit any significant spectral peaks at 13.5 and 9-day periods [Figs. 5(g) and 5(h)]. Thus, the results presented in Figs. 4 and 5 clearly indicate that these sub-harmonic solar

rotational periodicities at 13.5 and 9-day periods in geomagnetic activity indices (SymH and Kp) are primarily due to solar wind energy input associated with fast solar wind streams from the recurrent coronal holes. The solar wind high-speed streams (HSS) contain large-amplitude non-linear Alfvén waves within the CIRs [Tsurutani et al. 1994, Balogh et al. 1995]. The negative Bz components of the Alfvén waves within the high-speed streams lead to magnetic reconnection and transfer of energy from solar wind to the magnetosphere [Tsurutani and Gonzalez, 1987; Tsurutani et al. 2006], which is characterized by continuous auroral activity called as “High-Intensity Long Duration Continuous AE Activity (HILDCAA)”. The magnetic reconnection associated with the Alfvén waves cause continuous, shallow injections of solar wind plasma into the magnetosphere at auroral and mid latitudes. Further, the Kp-index which is a useful parameter to represent the particle precipitation at auroral and mid latitudes [Emery et al. 2008 and Emery et al. 2009] also exhibit coherent enhancements with SW velocity [Figs. 4(b) and 4(h)]. Therefore, the results from Figs. 4 and 5 clearly suggests that the fast solar wind trajectories from CHs, enhanced magnetic field associated with CIRs and Alfvén wave associated magnetic field fluctuations in HSS-CIR structures trigger recurrent geomagnetic activity of weak to moderate levels in the geo-space environment.

During the ascending phase and solar maximum, the high speed streams narrow and weaken because of poleward shrinkage of coronal holes (for example, as can be seen from Fig. 2(a)). Additionally, the ambient solar wind flow is frequently perturbed by energetic events on the Sun such as coronal mass ejections (CME) and solar flares. Hence, the CME-associated geomagnetic storms can occur more frequently near the solar maximum. Whereas the occurrence rate of HSS-CIR associated recurrent geomagnetic

storms maximizes during the declining phase and solar minimum [Tsurutani et al. 2006] due to the equatorward extended and/or low latitude isolated coronal holes as can be observed in Fig. 2(b). During the solar minimum in 2008, the Sun was exceptionally quiet with more than 70% of spotless days (annual average sunspot number was only 3) and global weakness in the heliospheric magnetic field [Gibson et al. 2009]. However, the large areas of low-mid latitude CHs and high speed streams [Figs. 4(a) and 4(b)] are persistent for several solar rotations resulting in recurrent HSS-CIR associated geomagnetic storms during 2008 [Fig. 4(g) and 4(h)]. It should be mentioned here that albeit the solar wind and geomagnetic activity indices are shown for only day numbers 1 to 120 in 2008 in Fig. 4 for better visibility, the HSS-CIR associated geomagnetic storms of moderate levels are observed almost throughout the year 2008 [for example, Lei et al. 2010].

### **2.3. The global ionospheric response to recurrent geomagnetic activity at quasi 9-day periods associated with HSS-CIR structures**

We now turn our investigation on the effects of this recurrent geomagnetic activity on the ionospheric electron density using the global vertical electron density observations of Formosat-3/COSMIC radio occultation measurements. The Formosat-3/COSMIC, in short F3/C, is a constellation of six micro satellites orbiting around 800 km altitude,  $72^\circ$  inclination angle, and  $30^\circ$  separation in longitude. Each F3/C satellite has a GPS Occultation eXperiment (GOX) payload, performing the radio occultation observations in the ionosphere and provides  $\sim 2000$  vertical electron density profiles per day which are uniformly distributed all over the globe. The details of inversion and validation of Ne(h) profiles can be found elsewhere [Schreiner et al. 1999 and 2007, Hajj

et al. 2000, Syndergaard et al. 2006 and Lei et al. 2007]. In the present study, the Ne(h) profiles during the entire year of 2008 were considered. All the vertical electron density profiles measured in each day are separated on solar local time (SLT) into day ( $06 \leq \text{SLT} < 18$  hrs) and night ( $18 \leq \text{SLT} < 06$  hrs of next UT day) time observations. The separated density profiles are then zonally (longitudinally) averaged into 32 latitudinal bins from  $-80^\circ$  to  $+80^\circ$  geomagnetic latitudes (with  $5^\circ$  window) and 30 altitudinal bins from 200 to 500 km (with 10 km window). The electron density profile data below 200 km were not considered in this study as the F3/C electron density data in the E- and F1-regions are often found to deviate from the ground based observations [Kelley, 2009, Liu et al. 2010]. Each binned time series of data are further spectral analyzed using the Lomb-Scargle (LS) algorithm to examine the periodicities in the zonal mean electron density.

For example, the zonal mean electron density at 300 km altitude during both day and night times are plotted as a function of geomagnetic latitude and day number in the year 2008, and presented in Figs. 6(a) and 6(b), respectively. The overlapped black curve in these figures is the variation of daily mean geomagnetic activity index, Kp in 2008. It can be seen from the Figs. 6(a) and 6(b), that the electron density exhibits large time scale seasonal and semi-annual variations as well as shorter time scale (multi-day) oscillations during both day and night times. Further, these shorter time scale oscillations in electron density corresponds well with the variations of daily mean geomagnetic activity index, Kp as may be seen from Figs. 6(a) and 6(b). In order to further examine the multi-day periodicities in the zonal mean electron density, Lomb-Scargle (LS) analysis is performed at each latitudinal bin and the periodograms are shown in Figs. 6(c) and 6(d) for day and night times, respectively. The LS periodogram of the daily mean geomagnetic activity

index, Kp is also overlapped (black curve with right hand scale) in Figs. 6(c) and 6(d) in order to examine the relationship between the periodicities in the electron density and the geomagnetic activity. Predominant spectral amplitudes are evident at solar rotational (27-day) and its sub-harmonic periods (13.5-day and 9-days) during both day and night times from  $-80^\circ$  to  $80^\circ$  geomagnetic latitudes. Further, the spectral amplitudes at these periodicities correspond extremely well with the periodicities in the geomagnetic activity index (Kp). Note that the EUV irradiance from TIMED SEE does not exhibit any significant spectral peaks at 13.5 and 9-day periods [Fig. 5(h)] during this period.

Thus, these results elucidate the periodic oscillations in both day and night side ionospheric electron densities at solar rotational and its sub-harmonic periodicities in support of earlier observations by Hocke [2008] and Lei et al. [2008c] in global mean total electron content (TEC). Hocke [2008] showed a perfect correlation in the 27 and 13.5-day oscillations between global mean TEC and solar EUV and further suggested that the other mechanisms rather than solar irradiation should contribute to the 9-, and 7-day periodicities as these periodicities are absent in solar EUV spectrum. Later, Lei et al. [2008c] have shown that the pronounced periodicities of 9- and 7-days in global mean TEC are associated with solar wind high speed streams and geomagnetic activity. Hence, the present results observed in the zonal mean electron density at 300 km corroborate with the results observed by Lei et al. [2008c] in global mean TEC. Although the 27-day and 13.5-day periodicities are present, they cannot be mainly attributed to recurrent geomagnetic activity as 27-day and 13.5-day periodicities also exist in F10.7 solar flux [Liang et al. 2008] which have a direct impact on the ion production. Therefore, we focus on the important feature of 9-day periodicity in electron density and Kp as a

diagnostic tool to investigate the global ionospheric response to HSS-CIR associated recurrent geomagnetic activity. There is also a significant peak observed at  $\sim 14$ -15 days in the electron density periodograms during both day and night times [Figs. 6(c) and 6(d)]. It can be speculated that this 14-15 day periodicity in the electron density could be possibly due to planetary wave oscillations in the lower thermosphere [Altadill and Apostolov, 2003]. Since the focus of current investigation is on sub-harmonic solar rotational periodicities, the spectral peak at  $\sim 14$ -15 day periodicity is not further discussed.

With a view to examine the phase relationship between the 9-day periodicities in the F-region ionosphere and the geomagnetic activity index (Kp) during different local times and seasons, the electron density oscillations corresponding to 9-day periodicities at each latitude-altitude bins are spectral filtered using a digital band pass filter centered at 9-days. Figure 7 shows the latitudinal variations of band pass filtered 9-day quasi-periodic perturbations in the electron density at 300 km altitude during both day times (left panels) and night times (right panels). The electron density perturbations corresponding to 45-days at each season are separately shown in Figs. 7a-f. Figures 7(a) and 7(b) correspond to day numbers 50-95 (equinox), Figures 7(c) and 7(d) correspond to day numbers 155-200 (June solstice) and Figures 7(e) and 7(f) correspond to day numbers 300-345 (December solstice). The day numbers in each season were carefully selected as the wavelet spectra of both solar wind velocity (Fig.1) and Kp-index (not shown in figure) exhibit strong spectral amplitudes at 9-day periodicity during those days. The overlapped black curve in each panel is the bandpass filtered 9-day perturbations in the Kp-index during the respective days. The perturbations in electron

density are expressed in relative percentage with respect to background levels (11-day running averaged electron density). From Fig. 7, it can be noticed that the amplitudes of electron density perturbations are slightly larger during the night than during the day. Also, the density perturbations are larger in the winter hemisphere than in the summer hemisphere and often exceed 40% of background levels. The larger percentage density perturbations could be due to smaller background electron densities during the night and at respective winter hemispheres as can be observed from Figs. 6(a) and 6(b).

Interestingly, the latitudinal variations in the band pass filtered electron density perturbations exhibit different phase relationship with the perturbations in Kp during different seasons. One consistent feature that can be observed during all the seasons is that the electron density perturbations are in-phase with the perturbations in Kp at low latitudes and out-of-phase at high latitudes during both day and night. This latitudinal variation is consistent with the changes in  $\Sigma O/N_2$  ratio observed by Crowley et al. [2008],  $N_m F_2$  variations observed by Tulasi Ram et al. [2010] and night time total electron content variations observed by Pedatella et al. [2010]. However, the latitudinal extent in which the electron density perturbations exhibit in-phase/out-of-phase relationship with Kp exhibits significant seasonal and local time dependence. During the equinox, the electron density perturbations are in-phase with Kp at low and mid-latitudes (0 to  $\pm 40^\circ$  geomagnetic latitudes), which then smoothly varies with latitude and become out-of-phase with Kp at high latitudes ( $\pm 60^\circ$  to  $\pm 80^\circ$  geomagnetic latitudes) during day times [Fig. 7(a)]. During night times, the negative phase relationship at high latitudes appears to extend into low latitudes in the southern hemisphere [Fig. 7(b)]. During the June solstice, the density perturbations are clearly out-of-phase in the summer (northern)

hemisphere above  $+40^{\circ}\text{N}$  geomagnetic latitudes during the day [Fig. 7(c)] and almost from geomagnetic equator during the night [Fig. 7(d)]. On the other hand, the density perturbations in the winter (southern) hemisphere exhibit in-phase relationship with  $K_p$  up to  $60^{\circ}\text{S}$  geomagnetic latitudes during both day and night. During the December solstice, the perturbations are in-phase between  $40^{\circ}\text{S}$  and  $40^{\circ}\text{N}$  geomagnetic latitudes and are out-of-phase at high latitudes ( $\pm 60^{\circ}$  to  $\pm 80^{\circ}$  geomagnetic latitudes) during the day [Fig. 7(e)]. Where as at night times, the negative phase zone penetrates deep in to low latitudes in the summer (southern) hemisphere and the same is confined to higher latitudes ( $65\text{--}80^{\circ}\text{N}$ ) in the winter (northern) hemisphere [Fig. 7(f)].

Figure 8 is similar to that of Fig. 7 except at a different height of 450 km altitude. It can be noticed that the latitudinal variation of electron density perturbations and their phase relationship with  $K_p$  at 450 km is quite different from that at 300 km. At 450 km altitude [Fig. 8], the electron density perturbations are in-phase with the perturbations in  $K_p$  and the negative phase relationship is mostly confined to high latitudes of summer hemisphere. During the equinoxes [Figs. 8(a) and 8(b)], the density perturbations exhibit in-phase relationship with  $K_p$  almost at all latitudes. These results indicate that the ionospheric electron density response to 9-day quasi periodic geomagnetic activity is not globally symmetric unlike the thermospheric mass density response as shown by Lei et al. [2008b] and Thayer et al. [2008]. Instead, the ionospheric response exhibits significant variation with latitude, altitude, local time as well as with season.

It was known that the upwelling neutral winds during geomagnetic storms carries molecular-rich air across the pressure level to higher altitudes leading to the reduction in  $\text{O}/\text{N}_2$  density ratio at high latitudes [Fuller-Rowell et al. 1994]. Also, the downwelling



wind transports atomic-oxygen-rich air parcels to low altitudes and enhances the O/N<sub>2</sub> density ratio at low latitudes [Strickland et al. 2001]. Thus, the out-of-phase (negative) response at high latitudes and in-phase (positive) response at low latitudes observed at 300 km [Fig. 7] can be attributed as due to changes in the storm time composition disturbances due to upwelling/downwelling at high/low latitudes [Crowley et al. 2008]. Further, the results from Figs. 7 and 8 indicates that the region of disturbed composition zone (negative phase response) penetrates deep into lower latitudes at 300 km (around F2-layer peak altitudes) and limits to higher latitudes at 450 km (topside ionosphere). Also, the latitudinal extent of composition disturbance zone is found to vary with local time as well as with season [Figs. 7 and 8].

In order to examine up to what latitudinal and altitudinal extent that the composition changes may affect during different seasons and local times, we proceed with the cross correlation analysis. The bandpass filtered 9-day periodic perturbations in electron density at each latitude-altitude bin are cross correlated with the perturbations in Kp and the zero-lag correlation coefficient is plotted as a function of latitude and altitude during the respective seasons and local times as shown in Fig. 9. The positive correlation coefficient indicate the enhancements in the electron density coherently with the enhancements in the geomagnetic activity (positive response) and the negative correlation indicate the reduction in electron density in response to enhanced geomagnetic activity (negative response). It can be seen from this figure that the correlation coefficient in the topside ionosphere (above 350 km) is positive except at high latitudes of northern summer hemisphere. The positive response in the topside ionosphere can be attributed to the thermal expansion of upper atmosphere and subsequent increase in the scale height

resulting from the enhanced plasma temperatures [Lei et al. 2008c, Sojka et al. 2009 and Tulasi Ram et al. 2010]. Further, it can be noticed from Fig. 9 is that the latitudinal and altitudinal extent of negative phase response due to disturbed neutral composition shows significant seasonal and local time dependence. One prominent feature that can be observed from Figs. 9(c)-(f) is that the region of negative correlation extends in to low and equatorial latitudes in the summer hemisphere during both the day and night times. Where as in the winter hemisphere, the negative correlation region is limited to high latitudes ( $> \sim 60^\circ$ ) during the day [Figs. 9(c) and 9(e)] and confined only to polar region during the night times [Figs. 9(d) and 9(f)]. These results clearly suggests that the disturbed composition changes due to upwelling winds at high latitudes penetrates deeper into low and equatorial latitudes in the summer hemisphere than in the winter hemisphere.

When the Joule and particle heating occur at high latitudes during the geomagnetic activity associated with recurrent high speed solar wind forcing, the heated thermosphere expands and leads to an increase in the neutral scale height ( $kT/mg$ ). While the larger effect is at high latitude, the atmospheric pressure tends to equilibrate globally, the corresponding expansion occurs at all latitudes. Recently, Sojka et al [2009] have shown that the ion temperature measured at 300 km shows strong enhancements associated with CIRs in high speed solar wind streams. Plasma temperature changes would cause similar changes in the plasma scale height, which is a measure of thickness of the ionosphere. The increase in the scale height due to thermal expansion associated with plasma temperature will cause similar increase in the F2-layer peak altitudes ( $h_m F2$ ). For example, Tulasi Ram et al. [2010] have also shown the 9-day quasi periodic

enhancements in the daytime topside ionospheric thickness ( $H_T$ ) and the F2-layer peak altitude ( $h_mF2$ ) coherently with the geomagnetic activity ( $K_p$ ) at all latitudes. Therefore, when one measures the electron density at any fixed height in the topside ionosphere, the increase/decrease in the scale height and  $h_mF2$  causes corresponding increase/decrease of electron density. Thus, the observed positive response in the topside ionosphere (above 350 km altitude) in Fig. 9 is related to corresponding changes in the scale height and  $h_mF2$  due to thermal expansion associated with plasma temperature. Further, the equatorward wind during enhanced geomagnetic activity will also raise the F-layer to higher altitudes. This would also contribute to the coherent enhancements in the  $h_mF2$  as observed by Tulası Ram et al. [2010]. However, the upwelling wind during enhanced geomagnetic activity carries the molecular rich air to higher altitudes at the same time leading to a decrease in  $O/N_2$  ratio. The electron density near F2-layer peak altitudes is mostly determined by the balance of production due to photoionization of O and loss due to  $N_2$  [Rishbeth and Garriott, 1969]. Thus, the electron density at F2 peak altitudes responds to changes in neutral composition ( $O/N_2$  density ratio) brought about by the upwelling/downwelling winds at high/low latitudes during the enhanced geomagnetic activity. The dominant process driving the electron density changes in the night time ionosphere is the loss through recombination. Thus, the changes in  $N_2$  and  $O_2$  concentrations due to upwelling will modify the chemical loss rates and in turn electron densities. Therefore, the electron density response around 200 to 350 km is dominated by the changes in neutral composition brought about by the global thermospheric circulation.

Further, there will be a mean transequatorial neutral wind from the summer hemisphere to winter hemisphere during the solstices. Also, the summer-to-winter

transequatorial neutral wind maximizes during the night due to reduced ion-drag. The summer-to-winter hemispheric wind will be in same direction to the equatorward wind in the summer hemisphere. On the other hand, the summer-to-winter hemispheric wind is in the opposite direction to the equatorward wind in the winter hemisphere. Thus, the latitudinal and altitudinal extent of disturbed composition changes observed in Fig. 9 depends on the relative strengths and directions of the summer-to-winter transequatorial wind and the equatorward wind due to high latitude heating during the periods of enhanced geomagnetic activity [Buansanto 1999]. In the summer hemisphere, the total wind is augmented by the prevailing summer-to-winter transequatorial wind and thus causes the composition disturbance zone to extend deep into low and equatorial latitudes as may be seen from Figs. 9(c)-(f). However, the summer-to-winter wind impedes the equatorward motion of the composition changes in the winter hemisphere. Thus, the negative phase response in the winter hemisphere is limited to high latitudes ( $\sim 60^\circ$ ) during the day time [Figs. 9(c) and 9(e)]. Further, the disturbed composition zone is limited only to polar region during the night time [Figs. 9(d) and 9(f)]. This could be possibly due to large oppositely acting transequatorial summer-to-winter winds during the night times.

### 3. Summary

A comprehensive investigation on the solar rotational and its sub-harmonic periodicities in coronal hole regions and solar wind velocity has been carried out, for the first time, using the solar EUV image data from the complete solar cycle 23 and its impact on the Earth's geomagnetic and ionospheric electron density have been studied

during the extreme solar minimum period, 2008. The important observations and results are herein summarized in the following paragraphs.

Both the solar wind velocity [Fig. 1(a)] and fractional CH area [Fig. 3(a)] consistently exhibit similar features with large values during the declining phase and the minimum of SC 23 indicating that the equatorward extension of polar holes and low-latitude (probably isolated) holes are prevailing during the declining phase of SC 23 (i.e., from 2003-2009). Further, both the SW velocity as well as the CH area exhibit greater tendency for sub-harmonic (13.5-day and 9-day) periodicities during the declining phase and minimum of SC 23. This suggests two/three large CH regions that longitudinally distributed by  $180^{\circ}/120^{\circ}$  apart and persistent for several rotations may produce sub-harmonic periodicities in the fractional CH area. This feature is more prominent during the declining phase and solar minimum because of the equatorward extension of polar holes or low-latitude isolated holes. Even though the previous solar minimum (1996-1998) period has the nearly the same solar activity (F10.7 solar flux) levels as the minimum of SC 23 (2005-2009), the values of both CH area and SW velocity are smaller during the previous solar minimum and the sub-harmonic periodicities are only occasionally observed for short periods [Figs. 1 and 3]. This speculates that the frequently observed, long lasting (several solar rotations) sub-harmonic periodicities in CH area and SW properties during the declining phase from 2003 to 2009 [Figs. 1(b) and 3(b)] may probably be a unique feature of SC 23. The recurrent solar wind high speed streams (HSS) from the several rotations of equatorward extended or low-latitude (probably isolated) coronal holes interact with the preceding ambient slow solar wind stream and produce recurrent co-rotating interaction regions (CIRs). The resultant HSS-

CIR structures of enhanced density and magnetic field regions recurrently impinge upon the Earth's magnetosphere. The magnetic reconnection associated with the Alfvén waves in the HSS-CIR structures cause continuous, shallow injections of solar wind plasma into the magnetosphere and trigger recurrent geomagnetic activity of weak to moderate levels in the geo-space environment [Fig. 4]. Further, the LS amplitude spectra [Fig. 5] of CH area, SW parameters and geomagnetic activity indices (SymH and Kp) show similar features with strong spectral peaks at 13.5 and 9-day periods. The results from Figs. 4 and 5 clearly suggest that the sub-harmonic solar rotational periodicities in the geomagnetic activity (SymH and Kp indices) are primarily due to solar wind energy input associated with CIR structures within the fast solar wind streams from the recurrent coronal holes.

The ionospheric electron density response to this HSS-CIR induced recurrent geomagnetic activity has been investigated using the Formosat-3/COSMIC radio occultation measurements during the extremely low solar activity year 2008. From Fig. 7, it was elucidated that the both day and night side electron densities exhibit periodic oscillations at solar rotational (27-day) and its sub-harmonic periodicities (13.5 and 9-day) in the electron density. Further, the spectral amplitudes of these oscillations in ionospheric electron density correlate well with the oscillations in the geomagnetic activity index, Kp. The important feature of 9-day periodicity in electron density and Kp is considered as a diagnostic tool to investigate the global ionospheric response to HSS-CIR associated recurrent geomagnetic activity. In general, the topside ionospheric response (above 350 km) appears to be dominated by the changes in the plasma temperature and/or scale height and exhibits coherent enhancements with the

perturbations in the Kp during both the day and night times. However, the electron density response between 200 and 350 km altitudes is dominated by the changes in the neutral composition and exhibits significant latitudinal, local time and seasonal variations. The upwelling winds at high latitudes significantly alters the neutral composition ( $O/N_2$  density ratio) and results in a decrease in electron density during the enhanced geomagnetic activity. In the summer hemisphere, the composition disturbance zone penetrates deep into low and equatorial latitudes during both day and night times where the total wind is augmented by the summer-to-winter transequatorial wind. In the winter hemisphere, the summer-to-winter wind is in the opposite direction and limits the composition disturbance zone to high latitudes ( $> \sim 60^\circ$ ) during the day time. Further, the enhanced transequatorial summer-to-winter wind during the night time restricts the composition disturbance zone only to polar region of winter hemisphere.

The recurrent geomagnetic disturbances associated with co-rotating interaction regions (CIR) in the solar wind high speed streams during the extreme solar minimum period, 2008 facilitates an opportunity to investigate the diurnal and seasonal dependence of the ionospheric response at different latitude and altitude regions. The results obtained from this investigation can be applicable to the global ionospheric response to minor (isolated) geomagnetic storms and thus provide some important insights to future modeling works on the ionosphere-thermosphere response to geomagnetic storms and solar wind-magnetosphere-ionosphere-thermosphere coupling processes.

#### 4. Acknowledgements

S. Tulasi Ram is supported by post-doctoral fellowship from ASIAA, Academia Sinica. The authors acknowledge Prof. Xuepu Zhao and Prof. S. T. Wu for their useful

discussion and Dr. Jiuhou Lei for providing great help in the wavelet analysis. Further, we thank the two reviewers for their constructive comments and suggestions which greatly helped in improving the paper. The authors wish to thank UCAR/CDAAC, NSPO for providing FORMOSAT-3/COSMIC data. The authors also acknowledge the open data policy of SOHO-EIT, STEREO-EUV teams for solar image data, ACE Science Center and NSSDC for SW data, WDC for geomagnetic data, SORCE team for TSI data and TIMED-SEE team for EUV irradiance data.

## 5. References

- Altadill, D., and E. M. Apostolov (2003), Time and scale size of planetary wave signatures in the ionospheric F region: Role of the geomagnetic activity and mesosphere/lower thermosphere winds, *J. Geophys. Res.*, 108(A11), 1403-1415, doi:10.1029/2003JA010015.
- Balogh, A., E. J. Smith, B. T. Tsurutani, D. J. Southwood, R. J. Forsyth, and T. S. Horbury (1995), The heliospheric magnetic field over the south polar region of the sun, *Science*, 268 (5218), 1007-1010.
- Buonsanto, M. J., (1999), Ionospheric Storms - A Review, *Space Sci. Rev.*, 88, 563-601.
- Choi, Y., Y.-J. Moon, Seonghwan Choi, Ji-Hye Baek, Sungsoo S. Kim, K.-S. Cho, and G.S. Choe (2009), Statistical Analysis of the Relationships among Coronal Holes, Corotating Interaction Regions, and Geomagnetic Storms, *Sol. Phys.*, 254, 311-323, doi:10.1007/s11207-008-9296-3.
- Crowley, G., A. Reynolds, J. P. Thayer, J. Lei, L. J. Paxton, A. B. Christensen, Y. Zhang, R. R. Meier, and D. J. Strickland (2008), Periodic modulations in thermospheric composition by solar wind high speed streams, *Geophys. Res. Lett.*, 35, L21106,



doi:10.1029/2008GL035745.

- Emery, B. A., V. Coumans, D. S. Evans, G. A. Germany, M. S. Greer, E. Holeman, K. Kadinsky-Cade, F. J. Rich, and W. Xu (2008), Seasonal, Kp, solar wind, and solar flux variations in long-term single-pass satellite estimates of electron and ion auroral hemispheric power, *J. Geophys. Res.*, 113, A06311, doi:10.1029/2007JA012866.
- Emery, B. A., I. G. Richardson, D. S. Evans, and F. J. Rich (2009), Solar wind structure sources and periodicities of auroral electron power over three solar cycles, *J. Atmos. Sol. Terr. Phys.*, 71, 1157-1175.
- Fuller-Rowell, T. J., M. V. Coderscu, H. Rishbeth, R. J. Moffett, and S. Quegan (1996), On the seasonal response of the thermosphere and ionosphere to geomagnetic storms, *J. Geophys. Res.*, 101, 2343-2353.
- Fuller-Rowell, T. J., M. V. Codrescu, R. J. Moffett, and S. Quegan (1994), Response of the thermosphere and ionosphere to geomagnetic storms, *J. Geophys. Res.*, 99, 3893–3914.
- Gibson, S. E., J. U. Kozyra, G. de Toma, B. A. Emery, T. Onsager, and B. J. Thompson (2009), If the Sun is so quiet, why is the Earth ringing? A comparison of two solar minimum intervals, *J. Geophys. Res.*, 114, A09105, doi:10.1029/2009JA014342.
- Hajj, G. A., L. C. Lee, Xiaoqing Pi, L. J. Romans, W. S. Schreiner, P. R. Straus, Chunming Wang (2000), COSMIC GPS Ionospheric Sensing and Space Weather, *Terr. Atmos. and Oceanic. Sci.*, 11(1), 235-272.
- Hocke, K. (2008), Oscillations of global mean TEC, *J. Geophys. Res.*, 113, A04302, doi:10.1029/2007JA012798.

- Kelley, M. C., V. K. Wong, N. Aponte, C. Coker, A. J. Mannucci, and A. Komjathy (2009), Comparison of COSMIC occultation-based electron density profiles and TIP observations with Arecibo incoherent scatter radar data, *Radio Sci.*, 44, RS4011, doi:10.1029/2008RS004087.
- Kennel, C. F., J. Arons, R. Blandford, F. Coroniti, M. Israel, L. Lanzerotti, A. Lightman, K. Papadopoulos, R. Rosner, and F. Scarf (1985), Perspectives on Space and Astrophysical Plasma Physics, Unstable Current Systems and Plasma Instabilities in Astrophysics, *IAU Symp.* (eds. M.R. Kundu and G.D. Holman), 537-552.
- Krieger, A. S., A. F. Timothy, and E. C. Roelof (1973), A coronal hole and its identification as the source of a high velocity solar wind stream, *Sol. Phys.*, 29, 505–525.
- Krista, L. D., and P. T. Gallagher (2009), Automated coronal hole detection using the local intensity thresholding techniques, *Sol. Phys.*, 256, 87-100, doi:10.1007/s11207-009-9357-2
- Lei, J., et al. (2007), Comparison of COSMIC ionospheric measurements with ground-based observations and model predictions: Preliminary results, *J. Geophys. Res.*, 112, A07308, doi:10.1029/2006JA012240.
- Lei, J., J. P. Thayer, J. M. Forbes, E. K. Sutton, and R. S. Nerem (2008a), Rotating solar coronal holes and periodic modulation of the upper atmosphere, *Geophys. Res. Lett.*, 35, L10109, doi:10.1029/2008GL033875.
- Lei, J., J. P. Thayer, J. M. Forbes, E. K. Sutton, R. S. Nerem, M. Temmer, and A. Veronig (2008b), Global thermospheric density variations caused by high-speed solar

- wind streams during the declining phase of solar cycle 23, *J. Geophys. Res.*, 113, A11303, doi:10.1029/2008JA013433.
- Lei, J., J. P. Thayer, J. M. Forbes, Q. Wu, C. She, W. Wan and W. Wang (2008c), Ionosphere response to solar wind high-speed streams, *Geophys. Res. Lett.*, 35, L19105, doi:10.1029/2008GL035208.
- Lei, J., J. P. Thayer, W. Wang, R. L. McPherron (2010), Impact of CIR storms on Thermosphere density variability during the solar minimum of 2008, *Sol. Phys.*, doi:10.1007/s11207-010-9563-y, in press.
- Liang, M.-C., K.-F. Li, R.-L. Shia, and Y. L. Yung (2008), Short-period solar cycle signals in the ionosphere observed by FORMOSAT-3/COSMIC, *Geophys. Res. Lett.*, 35, L15818, doi:10.1029/2008GL034433.
- Liu, J. Y., C. Y. Lin, C. H. Lin, H. F. Tsai, S. C. Solomon, Y. Y. Sun, I. T. Lee, W. S. Schreiner, and Y. H. Kuo (2010), Artificial Plasma Cave in the Low-latitude Ionosphere Results from the Radio Occultation Inversion of the FORMOSAT-3/COSMIC, *J. Geophys. Res.*, doi:10.1029/2009JA015079 (in press).
- Lomb, N. R. (1976), Least-squares frequency analysis of unequally spaced data, *Astrophys. Space Sci.*, 39, 447–462.
- McPherron, R.L., D. N. Baker, N. U. Crooker (2009), Role of the Russell – McPherron effect in the acceleration of relativistic electrons. *J. Atmos. Solar-Terr. Phys.* 71, 1032-1044.
- Mendillo, M. (2006), Storms in the ionosphere: Patterns and processes for total electron content, *Rev. Geophys.*, 44, RG4001, doi:10.1029/2005RG000193.
- Mendillo, M., and K. Schatten (1983), Influence of solar sector boundaries on

- ionospheric variability, *J. Geophys. Res.*, 88(A11), 9145-9153.
- Munro, R.H. and G. L. Withbroe (1972), Properties of a coronal “hole” derived from extreme-ultraviolet observations, *Astrophys. J.* 176, 511-520.
- Mursula, K., and B. Zieger (1996), The 13.5-day periodicity in the Sun, solar wind, and geomagnetic activity: The last three solar cycles, *J. Geophys. Res.*, 101(A12), 27077-27090.
- Pedatella, N. M., J. Lei, J. P. Thayer, and J. M. Forbes (2010), Ionosphere response to recurrent geomagnetic activity: Local time dependency, *J. Geophys. Res.*, 115, A02301, doi:10.1029/2009JA014712.
- Phillips J. L., S. J. Bame, W. C. Feldman et al. (1995), Ulysses Solar Wind plasma observations at high southerly latitudes, *Science* 268 (5213), 1030-1033 (1995).
- Prolss, G. W. (1980), Magnetic storm associated perturbation of the upper atmosphere: Recent results obtained by satellite-borne gas analyzers, *Rev. Geophys.*, 18, 183–202.
- Reeves, E.M., W. H. Parkinson (1970), An atlas of extreme-ultraviolet spectroheliograms from OSO-IV, *Astrophys. J. Suppl.* 21.1, 181.
- Richardson, I. G. (2004), Energetic particles and corotating interaction region in the solar wind, *Space Sci. Rev.* 111, 267–376.
- Richardson, I.G., G. Wibberenz, H. V. Cane (1996), The Relationship Between Recurring Cosmic Ray Depressions and Corotating SolarWind Streams at  $\leq 1$  AU: IMP 8 and Helios 1 and 2 Anti-Coincidence Guard Rate Observations, *J. Geophys. Res.* 101, 13483-13496.
- Richardson, I.G., J. E. Mazur, G. M. Mason (1998), A comparison of recurrent energetic

- ion enhancements observed at Ulysses and at 1AU by IMP-8 and SAMPEX: Ulysses launch until following the first north polar passage, *J. Geophys. Res.* 103, 2115-2130.
- Rishbeth, H., and O. K. Garriott (1969), Introduction to Ionospheric Physics, pp. 1 – 331, Academic, New York.
- Scargle, J. D. (1982), Studies in astronomical time series analysis. II. Statistical aspects of spectral analysis of unevenly spaced data, *Astrophys. J.*, 263, 835– 853.
- Schreiner, W. S., S. V. Sokolovskiy, and C. Rocken (1999), Analysis and validation of GPS/MET radio occultation data in the ionosphere, *Radio Sci.*, 34, 949– 966.
- Schreiner, W., C. Rocken, S. Sokolovskiy, S. Syndergaard, and D. Hunt (2007), Estimates of the precision of GPS radio occultations from the COSMIC/FORMOSAT-3 mission, *Geophys. Res. Lett.*, 34, L04808, doi:10.1029/2006GL027557.
- Sheeley, N. R., Jr., and J. W. Harvey (1981), Coronal holes, solar wind streams, and recurrent geomagnetic disturbances during 1978 and 1979, *Sol. Phys.*, 70, 237–249.
- Sojka, J. J., R. L. McPherron, A. P. van Eyken, M. J. Nicolls, C. J. Heinselman, and J. D. Kelly (2009), Observations of ionospheric heating during the passage of solar coronal hole fast streams, *Geophys. Res. Lett.*, 36, L19105, doi:10.1029/2009GL039064.
- Strickland, D. J., R. E. Daniell, and J. D. Craven (2001), Negative ionospheric storm coincident with DE 1-observed thermospheric disturbance on October 14, 1981, *J. Geophys. Res.*, 106, 21,049– 21,062.
- Syndergaard, S., W. S. Schreiner, C. Rocken, D. C. Hunt, and K. F. Dymond (2006), Preparing for COSMIC: Inversion and analysis of ionospheric data products, in

Atmosphere and Climate: Studies by Occultation Methods, edited by U. Foelsche, G. Kirchengast, and A. K. Steiner, *Springer*, Berlin, 137–146.

Temmer, M., B. Vrsnak, and A. M. Veronig (2007), Periodic appearance of coronal holes and the related variation of solar wind parameters, *Sol. Phys.*, 241, 371–383, doi:10.1007/s11207-007-0336-1.

Thayer, J. P., J. Lei, J. M. Forbes, E. K. Sutton, and R. S. Nerem (2008), Thermospheric density oscillations due to periodic solar wind high-speed streams, *J. Geophys. Res.*, 113, A06307, doi:10.1029/2008JA013190.

Timothy, A.F., A. S. Krieger, G. S., Vaiana (1975), The structure and evolution of coronal holes, *Solar Phys.* 42, 135-156.

Tsurutani, B. T., and W. D. Gonzalez (1987), The cause of high intensity long-duration continuous AE activity (HILDCAAs): Interplanetary Alfvén wave trains, *Planet. Space Sci.*, 35, 405

Tsurutani, B. T., C. M. Ho, E. J. Smith, M. Neugebauer, B. E. Goldstein, J. S. Mok, J. K. Arballo, A. Balogh, D. J. Southwood, and W. C. Feldman (1994), The relationship between interplanetary discontinuities and Alfvén waves: Ulysses observations, *Geophys. Res. Lett.*, 21, 2267.

Tsurutani, B. T., E. Echer, F. L. Guarnieri, and J. U. Kozyra (2008), CAWSES November 7–8, 2004, superstorm: Complex solar and interplanetary features in the post-solar maximum phase, *Geophys. Res. Lett.*, 35, L06S05, doi:10.1029/2007GL031473.

Tsurutani, B. T., et al. (2006), Corotating solar wind streams and recurrent geomagnetic activity: A review, *J. Geophys. Res.*, 111, A07S01, doi:10.1029/2005JA011273.

- Tsurutani, B. T., W. D. Gonzalez, A. L. C. Gonzalez, F. Tang, J. K. Arballo, and M. Okada (1995), Interplanetary origin of geomagnetic activity in the declining phase of the solar cycle, *J. Geophys. Res.*, 100(A11), 21,717– 21,733.
- Tulasi Ram, S., J. Lei, S.-Y. Su, C.H. Liu, C. H. Lin and W. S. Chen (2010), Dayside ionospheric response to recurrent geomagnetic activity during the extreme solar minimum of 2008, *Geophys. Res. Lett.*, 37, L02101, doi:10.1029/2009GL041038.
- Vrs̃nak, B., M. Temmer, and A. M. Veronig (2007), Coronal holes and solar wind high-speed streams: I. Forecasting the solar wind parameters, *Sol. Phys.*, 240, 315– 330.
- Wiegmann, T., and S.K. Solanki (2004), Why are Coronal Holes Indistinguishable from the Quiet Sun in Transition Region Radiation? *Proc. SOHO 15 Workshop - Coronal Heating*, ESA SP-575, 35.

605

606

607

608

609

610

611

612

613

614

## Figure Captions

Fig. 1: (a) The daily mean variation of SW velocity (light blue) and F10.7 solar flux (pink) along with their 27-day running mean variations during the years from 1996 to 2010. (b) The Morlet wavelet spectrum of SW velocity. The horizontal pink dotted lines in Fig. 1(b) represent the periodicities corresponding to 27, 13.5, 9 and 6.8 days. The thin contour line in black color highlights the spectrum above the 95% significance level. The vertical white dotted lines in Fig. 1(b) indicate the cone of influence of the wavelet power spectrum. The spectral intensities vary from dark blue (lowest) to dark red (highest).

Fig. 2: Typical examples of SOHO-EIT images at 195 Å during the ascending phase (August 03, 2000) and descending phase (January 27, 2005) of the SC 23. Large and isolated coronal holes can be seen at low latitudes during the descending phase. CH regions on the Sun are identified by intensity thresholding and the fractional CH area within the central meridian slice of  $\pm 10^\circ$  heliographic longitudes and  $\pm 60^\circ$  heliographic latitudes (the area covered by pink contour line) is considered on each day.

Fig. 3: (a) The daily variation of fractional CH area (light blue) along with their 27-day running mean variations during the years from 1996 to 2010. (b) The Morlet wavelet spectrum of CH area. The horizontal pink dotted lines in Fig. 3(b) represent the periodicities corresponding to 27, 13.5, 9 and 6.8 days. The thin contour line in black color highlights the spectrum above the 95% significance level. The vertical white dotted lines in Fig. 1(b) indicate the cone of influence of



the wavelet power spectrum. The spectral intensities vary from dark blue (lowest) to dark red (highest).

Fig. 4: The quasi 9-day periodic variation of (a) Fractional CH area, (b) SW bulk velocity, (c) SW magnetic field magnitude, (d) SW proton temperature (e) SW proton density, (f) vertical component IMF Bz, (g) ring current index, SymH and (g) geomagnetic activity index, Kp during the extreme solar minimum period from day number 1 to 120 in 2008.

Fig. 5: The Lomb-Scargle (LS) amplitude spectra of (a) Coronal Hole area, (b) Solar Wind velocity, (c) Solar Wind magnetic field magnitude  $|B|$ , (d) vertical component IMF Bz, (e) Kp-Index, (f) Sym-H index, (g) Total Solar Irradiance, and (h) EUV irradiance at 50 – 105 nm during the extreme solar minimum year of 2008.

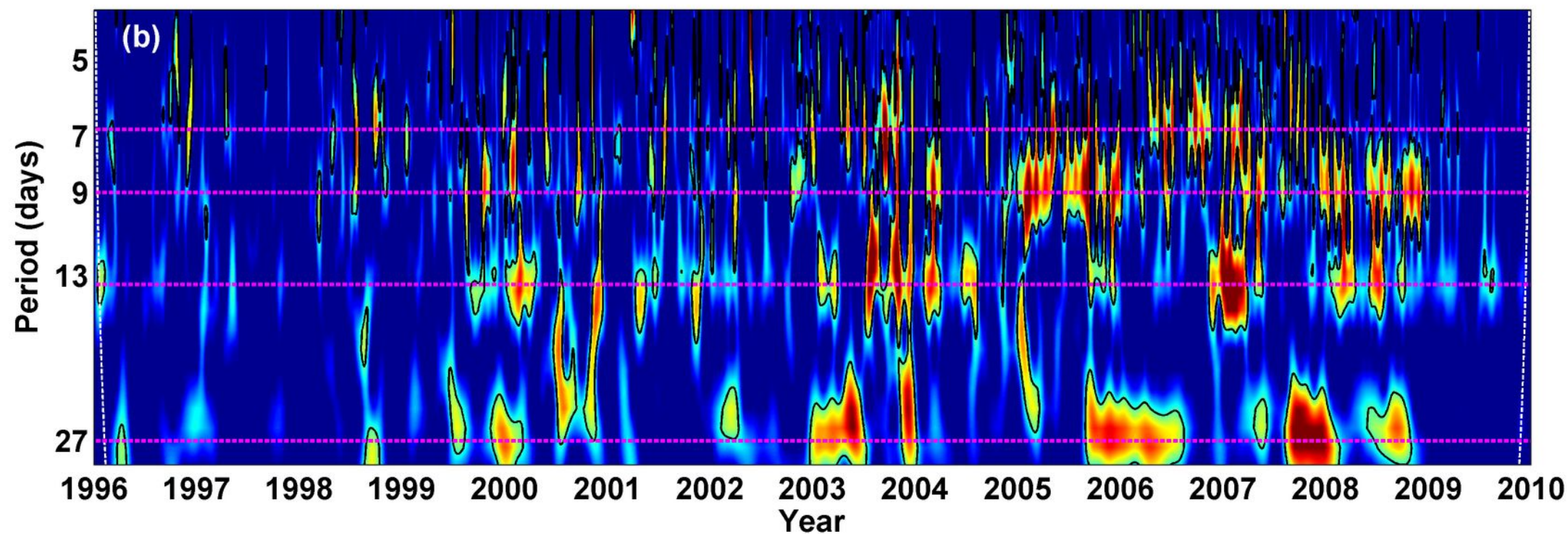
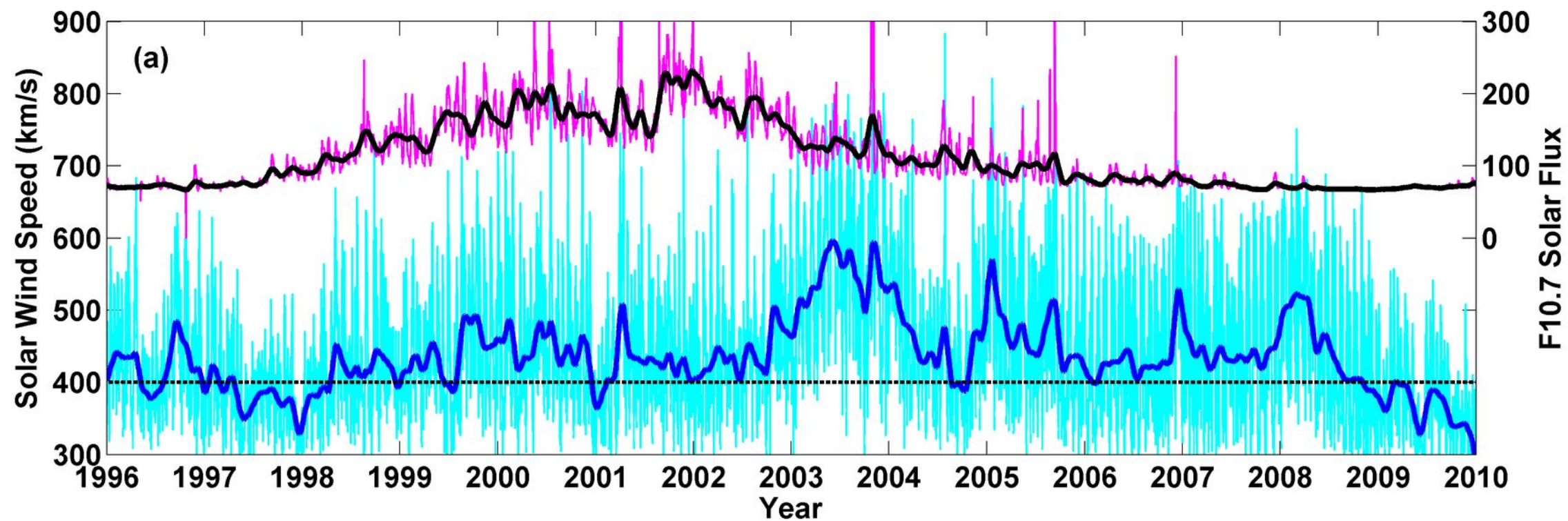
Fig. 6: The zonal mean electron density at 300 km altitude as a function of geomagnetic latitude and day number in 2008 during day [Fig. 6(a)] and night times [Fig. 6(b)]. The unit for electron density is  $\text{Ele}/\text{cm}^3$  in log scale. The corresponding Lomb-Scargle (LS) periodograms are shown in Figs. 6(c) and 6(d). Daily mean Kp-index and its LS spectral amplitudes are overlapped as black curves in the respective panels (right hand scale).

Fig. 7: Bandpass filtered 9-day quasi periodic perturbations in zonal mean electron density at 300 km altitude during equinoxes [Figs. 7(a) and 7(b)], northern summer [Figs. 7(c) and 7(d)] and northern winter solstices [Figs. 7(e) and 7(f)]. The left hand panels correspond to day time and right hand panels correspond to night time. The 9-day perturbations in Kp are also overlapped in each panel as

660           black curve with right hand scale. The electron density perturbations are  
661           expressed in percentage with respect to 11-day running mean.

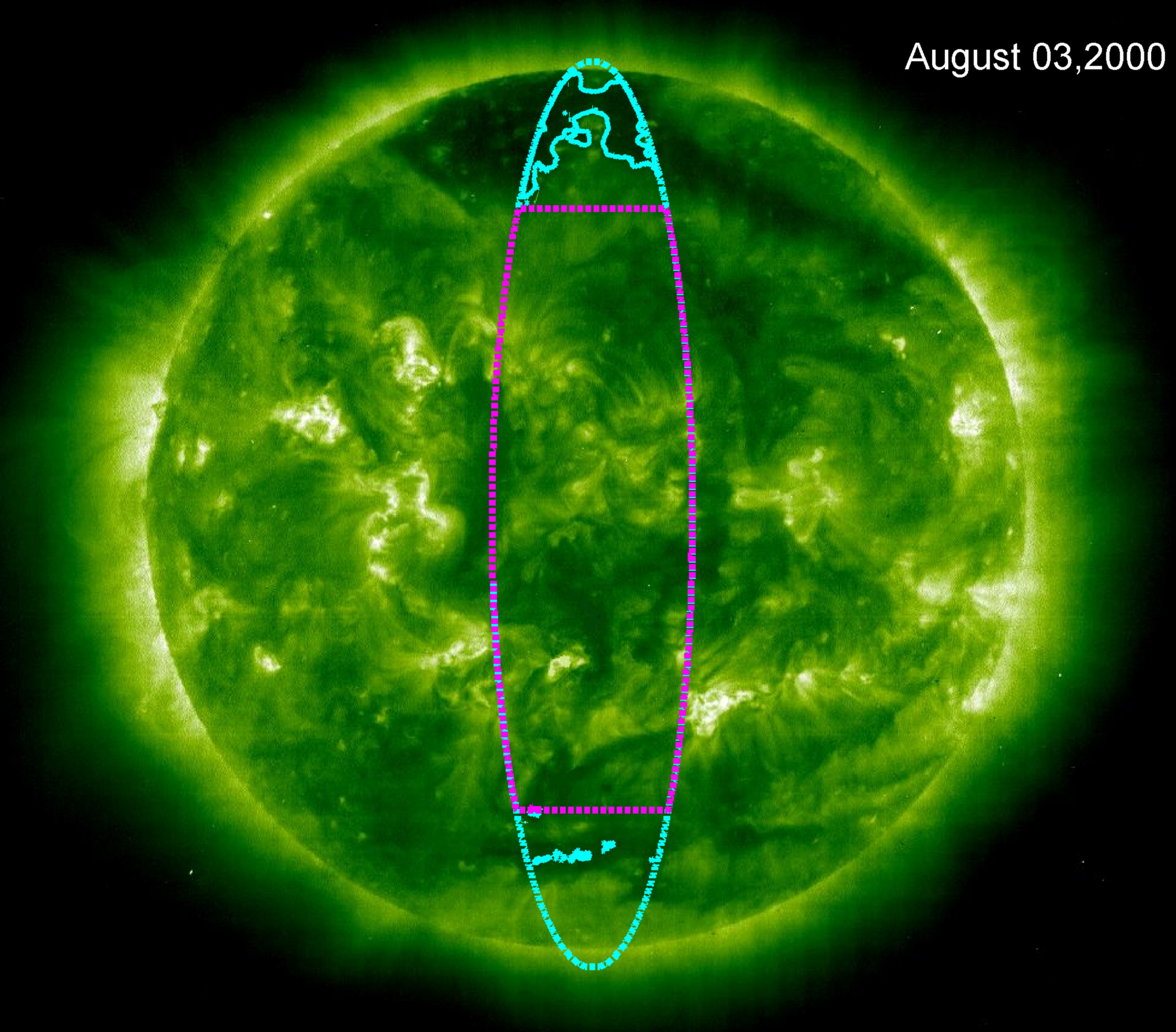
662   Fig. 8: Same as that of Fig. 7 except for 450 km altitude.

663   Fig. 9: (a) Latitudinal and altitudinal variation of correlation coefficient obtained from  
664           the cross correlation of bandpass filtered 9-day perturbations in electron density  
665           with the perturbations in Kp during equinoxes [Figs. 9(a) and 9(b)], northern  
666           summer [Figs. 9(c) and 9(d)] and northern winter solstices [Figs. 9(e) and 9(f)].  
667           The left hand panels correspond to day time and right hand panels correspond to  
668           night time.





August 03, 2000



January 27, 2005

